Atomic and electronic structure of exfoliated black phosphorus

Ryan J. Wu, Mehmet Topsakal, Tony Low, Matthew C. Robbins, Nazila Haratipour, Jong Seok Jeong, Renata M. Wentzcovitch, Steven J. Koester, and K. Andre Mkhoyan

Atomic and electronic structure of exfoliated black phosphorus

Ryan J. Wu and Mehmet Topsakal
Department of Chemical Engineering and Materials Science, University of Minnesota, Minneapolis, Minnesota 55455

Tony Low, Matthew C. Robbins, and Nazila Haratipour
Department of Electrical and Computer Engineering, University of Minnesota, Minneapolis, Minnesota 55455

Jong Seok Jeong and Renata M. Wentzcovitch
Department of Chemical Engineering and Materials Science, University of Minnesota, Minneapolis, Minnesota 55455

Steven J. Koester
Department of Electrical and Computer Engineering, University of Minnesota, Minneapolis, Minnesota 55455

K. Andre Mkhoyan[a]
Department of Chemical Engineering and Materials Science, University of Minnesota, Minneapolis, Minnesota 55455

Black phosphorus, a layered two-dimensional crystal with tunable electronic properties and high hole mobility, is quickly emerging as a promising candidate for future electronic and photonic devices. Although theoretical studies using *ab initio* calculations have tried to predict its atomic and electronic structure, uncertainty in its fundamental properties due to a lack of clear experimental evidence continues to stymie our full understanding and application of this novel material. In this work, aberration-corrected scanning transmission electron microscopy and *ab initio* calculations are used to study the crystal structure of few-layer black phosphorus. Directly interpretable annular dark-field images provide a three-dimensional atomic-resolution view of this layered material in which its stacking order and all three lattice parameters can be unambiguously identified. In addition, electron energy-loss spectroscopy (EELS) is used to measure the conduction band density of states of black phosphorus, which agrees well with the results of density functional theory calculations performed for the experimentally determined crystal. Furthermore, experimental EELS measurements of interband transitions and surface plasmon excitations are also consistent with simulated results. Finally, the effects of oxidation on both the atomic and electronic structure of black phosphorus are analyzed to explain observed device degradation. The transformation of black phosphorus into amorphous PO_3 or H_3PO_3 during oxidation may ultimately be responsible for the degradation of devices exposed to atmosphere over time. © *2015 American Vacuum Society.*
[http://dx.doi.org/10.1116/1.4926753]

I. INTRODUCTION

Black phosphorus received considerable scientific interest more than half a century ago due to its unusual stability compared to that of other phosphorus allotropes as a result of its unique crystal and electronic structure.[1–3] Recently, the emergence of two-dimensional (2D) materials[4,5] has led to a rediscovery of black phosphorus as a layered 2D material[6,7] with considerable applicability in electronics.[8,9] Possessing both a direct bandgap in a desirable range (0.3–2 eV)[10,11] and high hole mobility[7,12] gives this material a distinct advantage over graphene and transition metal dichalcogenides for applications in field-effect transistors (FETs) and other devices.[6,13] Similar to other layered 2D materials, black phosphorus possesses tunable electronic properties as a function of the number of layers present.[10,11] Furthermore, heterostructures of this material have also reportedly been used for diodes[14] and battery anodes[15] making black

phosphorus a promising candidate as a building block of future novel devices.[16]

The successful application of black phosphorus requires a thorough understanding of its crystal and electronic structure in both its bulk and thin-layer regimes. Early x-ray diffraction[1,17] and angle resolved ultraviolet photoelectron experiments[18] reported the first measurements of the lattice parameters, band structure, and stable stacking arrangement for bulk black phosphorus. Although many recent theoretical studies have been performed to study how these characteristics and properties may differ for atomically thin black phosphorus, relatively few experimental studies have followed to confirm these theoretical predictions. Techniques such as scanning tunneling microscopy,[19] atomic force microscopy (AFM),[6,20] conventional transmission electron microscopy (CTEM),[21,22] and Raman spectroscopy[22,23] have all contributed to the experimental characterization of atomically thin black phosphorus. However, these methods do not allow the direct three dimensional visualization of its atomic structure, nor do they simultaneously provide information on its electronic structure, both of which may be necessary to analyze

[a]Author to whom correspondence should be addressed; electronic mail: mkhoyan@umn.edu

the behavior of black phosphorus in its thinner regime. Therefore, an atomic-resolution approach is warranted to properly study the atomic and electronic structure of atomically thin black phosphorus.

In this work, analytical aberration-corrected scanning transmission electron microscopy (STEM) is used to record atomic-number sensitive (Z-contrast) annular dark-field (ADF) images of few-layer black phosphorus with atomic resolution to provide directly interpretable images of its layered crystal structure. Due to its high spatial resolution ($\sim$0.8 Å) and direct interpretability, as compared to phase-contrast imaging in CTEM, aberration-corrected STEM with ADF imaging serves as the ideal tool to characterize atomically thin black phosphorus. In addition, monochromated electron energy-loss spectroscopy (EELS) with 0.25 eV energy resolution is used in parallel with ADF-STEM to measure the valence transitions and conduction band density of states (DOS) of black phosphorus. These measurements are then compared with *ab initio* calculations to analyze the electronic structure. Complementary experimental EELS and theoretical modeling has been effectively employed to analyze the electronic structure of other layered materials such as graphene oxide,[24] graphene,[25] and boron nitride[26] but has yet to be performed for black phosphorus. The effects of oxidation on both the atomic and electronic structure of black phosphorus are also explored to explain previously reported device degradation at ambient conditions.[27,28]

II. EXPERIMENT

A. STEM sample preparation

Black phosphorus flakes were mechanically exfoliated from bulk crystals (99.998% pure from Smart Elements) and then transferred onto a PDMS (Corning Sylgard 184) stamp on a glass slide.[29] Thin flakes on the PDMS stamp were identified under an optical microscope and transferred onto a *Quantifoil* TEM grid (from Electron Microscopy Science) using a micropositioner. Both the black phosphorus exfoliation and subsequent transfer to the TEM grid occurred in atmosphere at approximately 70% relative humidity. The grid was then briefly (only for 5 s) plasma cleaned, using a Fischione 1070 NanoClean plasma cleaner, which uses a 30 sccm mixture of 75% Ar and 25% O_2 and immediately inserted into the STEM. The plasma cleaner was operated at 3.8 W forward power and 2 W reflected power. The total time that black phosphorus specimens were exposed to atmosphere during this sample preparation was less than 10 min. The PDMS stamping method of transfer inevitably introduces some oxygen via the siloxanes present in the PDMS polymer. The initial atomic percentage of oxygen is approximately 15% as measured by STEM-EDX, which results in 5%–10% error in the data, considering the threefold coordination of phosphorous, and should be treated as such.

B. STEM instrumentation and experimental conditions

A standard FEI Titan G2 60–300 aberration-corrected and monochromated STEM equipped with a CEOS DCOR probe corrector was used in this study. The microscope is also equipped with a Gatan Enfinium ER EEL spectrometer and SuperX EDX spectrometer for EELS and EDX collection, respectively. ADF-STEM images (2048 × 2048 pixel^2) were acquired on the STEM operating at 200 keV using a dwell time of 3–6 μs per image pixel at a camera length of 130 mm. The beam convergence angle, α_{obj}, was measured to be 23 mrad. The ADF detector inner and outer angles of collection were measured to be 54 and 317 mrad, respectively. Low- and core-loss EELS were collected at a camera length of 38 mm with $\alpha_{ob} = 17$ mrad and a collection angle $\beta = 26$ mrad. Under these conditions, the measured probe size was $\sim$0.8 Å. Core- and low-loss EELS were recorded using a dispersion of 0.05 and 0.01 eV/channel, respectively. The energy resolution measured using the FWHM of the zero-loss peak was 0.25 eV. The collection time in either case was 4–8 s per spectrum. Typically, 50 spectra were collected while repeatedly scanning over a 0.1×0.1 μm^2 area of the specimen and were summed together to obtain the final spectrum. STEM-EDX composition maps (1024 × 1024 pixel^2) were acquired in parallel from the P, Si, O, and C K x-ray peaks, with corresponding ADF-STEM images. Acquisition occurred while repeatedly scanning over the area for 15–20 min.

C. HAADF-STEM image processing

In order to improve signal to noise ratio, all HAADF-STEM images shown in Fig. 3 are low- and high-pass filtered, limiting the information below 0.6 Å and above 10 Å. In addition, the HAADF-STEM images in panels (a) and (b) were further processed by averaging 14 and 16 images, respectively, using a cross-correlation algorithm. The detailed image processing procedure can be found in the supplementary material.[30]

D. Device fabrication and testing procedure

Flakes on PDMS prepared as described above in *STEM sample preparation* were transferred onto a 290 nm SiO$_2$ layer on a Si substrate. Contacts spaced 2 μm apart were then patterned using electron beam lithography, and Ti (10 nm)–Au (90 nm) contacts were deposited using electron-beam evaporation. The total time that black phosphorus specimens were exposed to atmosphere before the first measurement was less than 2 h. Electrical measurements were performed every 30 min for an 8 h period using an Agilent B1500A semiconductor device parameter analyzer. The device degradation experiment was performed in ambient conditions at 70% relative humidity.

III. MODELING

A. Details of DFT calculations

Ab initio calculations were performed in the framework of density functional theory (DFT) as implemented in the Vienna *ab initio* Simulation Package code.[31,32] Electronic exchange and correlation effects were described using a hybrid functional (HSE06) introduced by Heyd, Scuseria, and Ernzerhof.[33] One quarter of the Perdew–Burke–Ernzerhof

(PBE) short-range exchange is replaced by exact exchange while the full PBE correlation energy[34] is included. This hybrid functional was shown to yield improved bandgaps compared to the PBE functional.[35,36] The Tkatchenko–Scheffler dispersion-correction scheme[37] was employed to account for the van der Waals (vdW)-type interactions between adjacent phosphorus layers. The interactions between ions and valence electrons are described by the projected augmented wave method[38] with a plane wave cutoff of 300 eV. The atoms were allowed to relax until the forces per ion were smaller than 0.005 eV/Å using the conjugate gradient method[39] in which the total energy and forces are simultaneously minimized. The Brillouin zone was sampled using $8 \times 6 \times 1$ shifted Monkhorst–Pack k-points for structural relaxations and a denser $18 \times 12 \times 1$ gamma-centered k-point grid with the tetrahedron method[40] was used for electronic structure calculations. A large spacing of 15 Å between the 2D layers is used to prevent interactions between them. Frequency dependent dielectric matrix calculated within random phase approximation after the electronic ground state has been achieved as detailed in Gajdoš *et al.*[41] The imaginary part is computed by a summation over 27 empty states per atom.

B. Calculating surface plasmon loss functions

The contribution of surface plasmon excitations in experimental low-loss EELS data is calculated by integration of the loss function $L_{jj}(q, E) = \text{Im}\{-1/\varepsilon_{jj}(q, E)\}$ multiplied by the scattering factor, $S(\vec{q})$, over all scattering events, limited only by STEM electron optics and detector geometry.[42] Here, the momentum transfer for probe electrons is defined as: $\hbar\vec{q} = \hbar\vec{k}_0 - \hbar\vec{k}'$, where $\hbar\vec{k}_0$ is incident and $\hbar\vec{k}'$ is scattered electron momenta. $\varepsilon_{jj}(q, E)$ is the tensor of two-dimensional dielectric function for a monolayer black phosphorous and was calculated using the Drude model with a quasistatic approximation.[43] The Drude weight, $D_j = \pi e^2 n / m_j$, is determined by estimating the carrier density, n, from the experimentally measured bulk plasmon energy, $E_P = 19.3$ eV and the electron effective masses are approximated as $m_a^* = 0.08 m_0$ and $m_b^* = 0.7 m_0$ for two in-plane directions.[44] The conversion of all parameters from momentum transfer to more convenient scattering angle, θ, was performed using the relation: $q^2 = k_0^2 (\theta^2 + \theta_E^2)$ where $\theta_E = E_{SP}/2\gamma m_o v_o^2$ is the characteristic surface plasmon scattering angle with relativistic correction, γ.[42] All parameters used in calculating $S(\theta, \theta_E)$ were based on the experimental microscope parameters discussed previously.

C. ADF-STEM image simulation parameters

ADF-STEM images of 2–4 layer black phosphorus samples were simulated using the multislice method[45] implemented with the code developed by Kirkland.[46] All simulations were performed for a STEM operating at 200 keV using an aberration-corrected probe with $C_{s(3)} = -0.001$ mm, $C_{s(5)} = 0.01$ mm, $\Delta f = 5$ Å, and $\alpha = 17$ mrad. These parameters were selected based on the experimental STEM conditions. The simulated beam has a full-width half-maximum (FWHM) of approximately 1 Å, which corresponds to a probe

size slightly larger than that experimentally demonstrated at this energy.[47] Image simulations were performed on a 44×32 Å^2 supercell using a transmission function and probe function calculated at 1024×1024 pixel.[2] The slice thickness was set as 2 Å. A simulated ADF detector collected electrons scattered 54–317 mrad off of the optic axis to form the image, in accordance with the experimental ADF detector. The effects of thermal displacements were simulated by averaging ten frozen phonons configurations at 300 K for each image (additional simulations showed that higher phonon configurations negligibly affected the ADF-STEM image considered here). The root mean square (rms) thermal displacement value used for phosphorus was 0.0745 Å. This value is selected as the average between referenced values of 0.071 Å for sulfur[48] and 0.078 Å for silicon.[46]

IV. RESULTS AND DISCUSSION

A. Identification of black phosphorus and thickness determination

Black phosphorus is susceptible to structural degradation when exposed to ambient O_2 and H_2O.[27,28,49] Although the mechanism is still not completely understood, the presence of light has also been shown to either initiate[21] or accelerate[28] this degradation. Thus, pristine black phosphorus samples were handled with minimal ambient and light exposure (see Sec. II), and prior compositional analyses were performed to ensure that the black phosphorus flakes selected for study were not significantly altered. Figure 1 shows low-
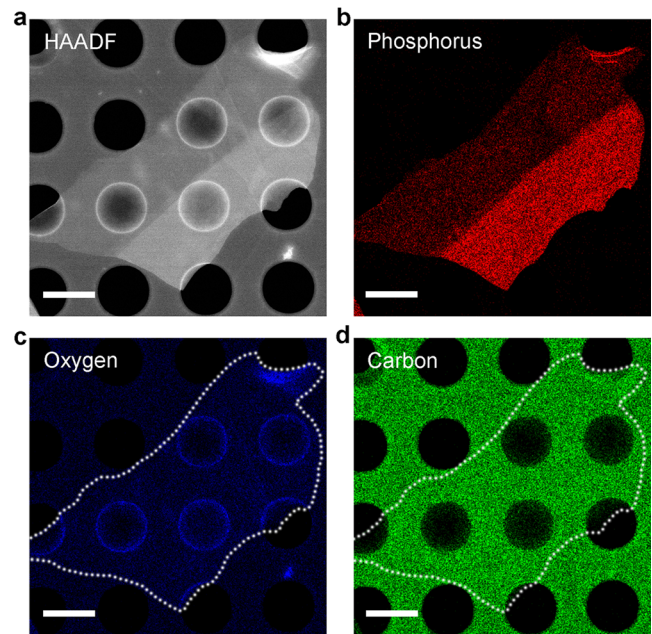

FIG. 1. (Color online) Energy dispersive x-ray spectroscopy maps of few-layer black phosphorus. (a) ADF-STEM image of a black phosphorus flake with thinner (four-layer) and thicker (eight-layer) regions deposited on an amorphous-carbon-coated TEM grid with 1 μm diameter holes. The brighter ADF-STEM signal corresponds to the thicker region. (b)–(d) Phosphorus, oxygen, and carbon EDX maps, respectively, recorded from the flake shown in (a). The white dotted borders in (c) and (d) have been used to highlight the position of the flake. The ADF-STEM image and all elemental EDX maps are acquired simultaneously. Scale bars are 1 μm.

magnification STEM energy dispersive x-ray spectroscopy (EDX) elemental maps of a representative black phosphorus flake that was prepared by mechanical exfoliation and quickly transferred into the STEM (see Sec. II). The ADF-STEM image [Fig. 1(a)], recorded simultaneously with the EDX maps, provides thickness contrast[50] in addition to Z-contrast. The thickness of the black phosphorus flake was estimated by comparing the ADF intensities of the flake to that of the amorphous carbon supporting film on the TEM grid as reference (see supplementary material). These estimates show that the thinner (darker) region in Fig. 1(a) consists of approximately four layers thick, whereas the thicker (brighter) region consists of approximately eight layers. The strong P intensity shown in Fig. 1(b) outlines the shape of the flake, as expected for black phosphorus, and the strong C signal in Fig. 1(d) outlines the amorphous carbon supporting film. Furthermore, the thicker region has approximately two-fold higher P intensity than the thinner region, which further confirms the thicker region is indeed approximately two times thicker. Significantly weaker O, C, and Si signals (see

supplementary material for Si map) observed in the location of the black phosphorus flake originate predominately from the PDMS (chemical formula: $[C_2H_6OSi]_n$) residue remaining from the STEM sample preparation (see Sec. II for additional details). The quantitative analysis of the STEM-EDX elemental maps (described in detail in supplementary material) shows that the flake transferred into the STEM is mainly pristine, and practically unoxidized black phosphorus.

B. Crystal structure of black phosphorus

1. Simulated crystal structure

Figure 2(a) shows a 3D rendered model of black phosphorus with AB-stacking in profile. A single layer of black phosphorus consists of two rows of P atoms with each P atom bonded to three adjacent neighbors, thereby forming six membered rings or a puckered structure.[8] In its bulk form, the layer-to-layer stacking order was determined[2,17] to be AB-stacked, where every other layer is shifted by a half unit cell along the [100] direction. Three alternative stacking
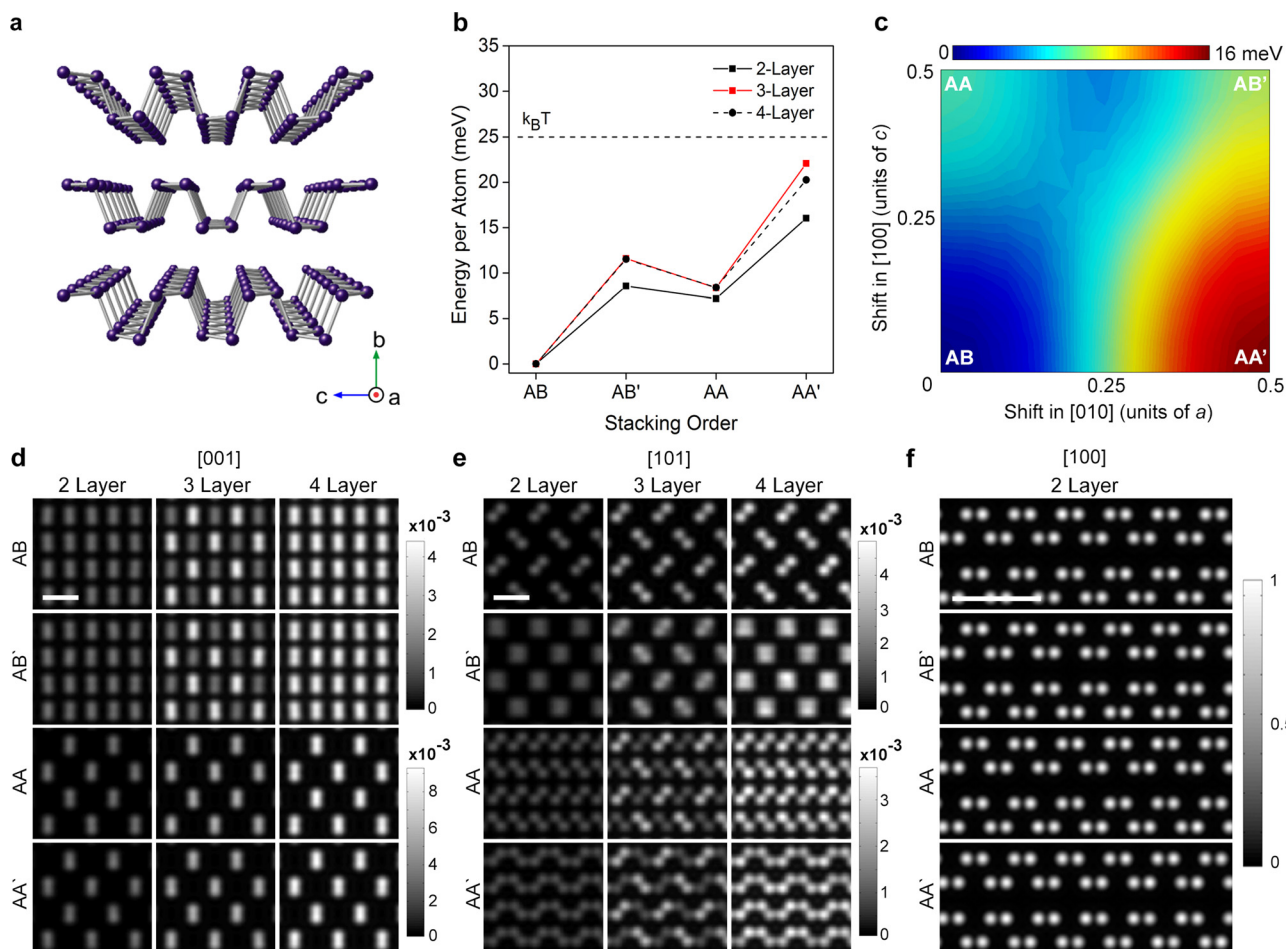

FIG. 2. (Color online) Calculated models of black phosphorus with various stacking orders. (a) Model of AB-stacked three-layers-thick black phosphorus showing its armchair nature. (b) DFT calculated energy comparison of two- to four-layers-thick black phosphorus samples with various stacking orders. Zero of the energy was set to the energy of AB-stacking. (c) Calculated contour map tracking the energy of a two-layers-thick black phosphorus sample as the top layer is shifted relative to the bottom layer. (d)–(f) *Multislice* simulated ADF-STEM images of two- to four-layers-thick black phosphorus with various stacking orders viewed along the [001], [101], and [100] crystallographic directions, respectively. Gray scale bars in (d) and (e) are scaled to each row with AA (AB) and AA (AB′) sharing the same intensity scale bar; absolute intensities are normalized to the incident beam. Intensity in (f) is normalized to the highest intensity in the simulated images. Scale bars in (d) and (e) are 4 Å, and the scale bar in (f) is 1 nm.

orders have also been proposed:[51] in AA stacking, the layers align directly on top of each other. In AA′ and AB′ stacking, every other layer is shifted by half a unit cell along the [010] and [110] directions, respectively. Figure 2(b) shows an *ab initio* calculation of the energies associated with the four stacking orders for 2–4 layers. The energetics show that AB-stacked black phosphorus remains the most favorable state even in 2–4 layers-thick cases. However, AA-, AA′-, and AB′-stacked black phosphorus all possess energies below 0.025 eV (or k_BT at room temperature) per atom, which suggests that they may be accessible at room temperature. The accessibility and stability of these alternate stacking orders depends mainly on the energy barrier preventing the transition from AA, AA′, and AB′ into AB stacking. Figure 2(c) shows an energy contour map of all possible shifts of the top layer relative to the bottom layer for simulated two-layer-thick black phosphorus. Using crystallographic directions, 0.5-unit-cell shifts relative to AB stacking in the [100], [010], and [110] directions brings the system into AA, AA′, and AB′ stacking, respectively. As shown in the contour map, no energy barrier exists for these alternate stacking orders to transition into AB-stacking. Therefore, pure AA-, AA′-, or AB′-stacked black phosphorus are unstable and would readily transform into AB-stacked. Interestingly, the contour map shows the presence of a metastable state at 0.25 shift in [010] and 0.5 shift in [100] with an energy barrier of ~2 meV. Such a small energy barrier, however, makes this metastable state exceptionally difficult to isolate, but it may be accessible under extremely low temperatures. Despite the overall instability of these other stacking orders, the presence of defects or strains in the crystal could allow them to be observed and isolated, as was demonstrated in the case of graphene.[52,53]

In the scenario that alternatively stacked black phosphorus is isolated (with defects or strains), ADF-STEM imaging can be used to discern the various stacked structures. To show this, ADF-STEM images were simulated for black phosphorus with various stacking orders [Figs. 2(d)–2(f)]. These images were generated using a ~1 Å electron probe, which can be routinely achieved in an aberration-corrected STEM (see Sec. III). Figure 2(d) presents simulated ADF-STEM images along the *c*-axis or [001] crystallographic direction for two to four-layer black phosphorus, in which spots of high intensity represent the locations of atomic columns or pairs of atomic columns, for two-to-four-layer black phosphorus along the *b*-axis, or the [001] crystallographic direction. Because of their half-unit-cell shift with each layer, AB- and AB′-stacked structures show intensities at *a*/2 and *c*/2 spacing between pairs of atomic columns, in contrast to AA and AA′-stacked structures that show only *a* and *c* spacing. Figure 2(d) also demonstrates that AA (AB)- and AA′ (AB′)-stacked black phosphorus cannot be unambiguously distinguished at this orientation. Figure 2(e) shows simulated ADF-STEM images of two- to four-layer thick black phosphorus viewed along the [101] zone axis (17° tilted from the [001]), and Fig. 2(f) shows images of two-layer thick black phosphorus along the [100] zone axis.

When viewed along the [101] zone axis, all four stacking orders create unique patterns that allow them to be distinguished. Furthermore, these unique patterns are consistent across all thicknesses. Finally, imaging along the [100] zone axis allows the AA and AA′ stacking orders and the AB and AB′ stacking orders to be distinguished from each other, due to the half a unit-cell shift along the [010] and [110] directions. Thus, ADF-STEM imaging can be applied to unambiguously determine the stacking order of black phosphorus.

2. Experimental crystal structure

Figure 3(a) shows an experimental ADF-STEM image of an exfoliated black phosphorus flake viewed along the [001] crystallographic direction where P atomic column pairs can be directly observed. Similar to simulated ADF-STEM images, experimental ADF-STEM images provide directly interpretable images with exact positions of the atomic columns shown as high intensity spots.[54] Figure 3(b) shows an ADF-STEM image of a different black phosphorus flake exfoliated from the same bulk sample viewed along the [101] direction. Here the increased spacing between atomic columns allows the individual atomic columns to be clearly visible. The ADF-STEM images captured along the [001] and [101] zone axes allow direct determination of the bulk black phosphorus lattice parameters, which have been measured to be $a = 3.31 \pm 0.03$ Å and $c = 4.34 \pm 0.05$ Å. These measured in-plane lattice parameters are in agreement with early experimental powder diffraction measurements[2,17] and other computational predictions[44,51,55] as summarized in Table I. Figures 3(c) and 3(d) show low- and high-magnification ADF-STEM images captured at the edge of a black phosphorus flake, which was aligned along the [100] crystallographic direction. This essentially provides a cross-sectional view of layered 2D black phosphorus. Folding of layered materials at the edges stabilizes the dangling bonds and has been previously reported on other layered materials such as graphene[56] and *h*-BN.[57] Using this image, the out-of-plane lattice parameter (*b*/2) is measured to be 5.4 ± 0.2 Å, which closely resembles a reported AFM result of 5.3 Å.[8]

The stacking order differentiation methods derived from the simulated ADF-STEM images can be directly applied to the experimental ADF-STEM images shown in Fig. 3. Figure 3(a) shows that the black phosphorus flake possesses *a*/2 and *c*/2 spacing when imaged along with [001] zone axes, which is unique to AB and AB′-stacking, as previously discussed. In addition, its image along the [101] zone axis [Fig. 3(b)] and its cross-sectional image [Fig. 3(d)] resembles the images simulated for AB-stacking [Figs. 2(e) and 2(f)]. Thus, altogether, the atomic-resolution images show that exfoliated black phosphorus shares the same AB-stacking order as bulk black phosphorus, which confirms the results of early powder diffraction experiments.[2,17] Furthermore, the good agreement between the complementary experimental and simulated results presented here show that the stacking order differentiation methods discussed previously can be used reliably.
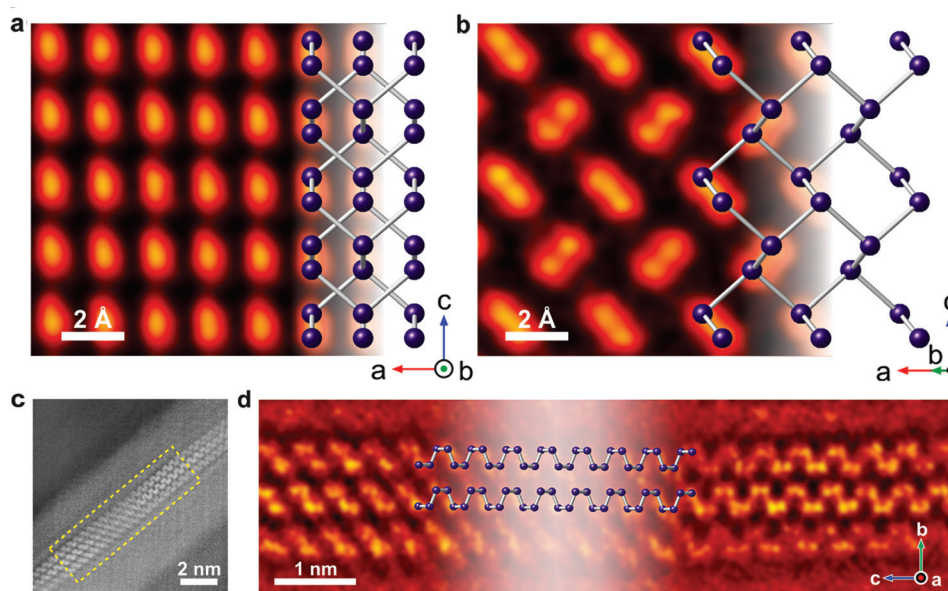
FIG. 3. (Color online) Atomic-resolution ADF-STEM images of black phosphorus. (a) ADF-STEM image of black phosphorus viewed along the [001] crystal-lographic direction, or top-down view, compared to a model. (b) ADF-STEM image viewed along the [101] direction or 17° tilted off the [001] zone axis. (c) ADF-STEM image captured at an edge of a black phosphorus flake showing multiple layers stacked together, or along the [100] direction. (d) Magnified image of the region highlighted in (d). Images in (a), (c), and (d) have overlaid ball-and-stick atomic models to accentuate the atomic columns. To improve the signal-to-noise ratio, the ADF-STEM images presented in (a), (b), and (d) were FFT-based low- and high-passed filtered; additionally, (a) and (b) were also cross-correlatively averaged across several images. It should be noted that all atomic-scale features uniquely identifying crystal structure are resolved in the raw images. Details of the images processing procedure can be found in Sec. II and supplementary material.

C. Electronic structure of black phosphorus

EELS data recorded from any area of a specimen in STEM can be directly compared with the specimen's local DOS, as it represents direct electronic transitions of atomic core-level electrons to the empty states above the Fermi energy, E_F.[58] Figure 4(a) shows the calculated total and partial DOS of the valence and conduction bands of four-layer and bulk black phosphorus to be compared with experimental EELS data (see Sec. III for the calculation procedure and supplementary material for calculated band structures). The calculated band gap, E_g, shown in the figure inset closely match those reported in literature.[59] At various points along the bands, the s-, p-, and d-orbital partial DOS contribute with different weights to the total DOS. The bottom of the conduction band (1–5 eV) has primarily p character, whereas the states beyond 5 eV possess both p and d character. Experimental EELS measurements of the P L_3 edge can be used to identify the combined s and d partial conduction band DOS. The P L_3 edge corresponds to electronic transitions from $2p^{3/2}$ to $3s$ and $3d$ in observance of dipole selection rules. Therefore, $3s$ and $3d$ orbital contributions to the conduction band can be compared directly with the experimental EELS P L_3 edge. Figure 4(b) shows that the P L_3 edge has an onset peak at 130.3 eV followed by a decrease in the DOS between 132 and 135 eV. The second set of peaks between 136 and 140 eV appears with a gradual increase in the DOS. The EELS peak positions, which indicate energies with high DOS in the conduction band, match well with those predicted by *ab initio* calculations. Minor discrepancies in the relative intensities of the peaks observed here are due to the "core-hole" effect, which was also observed between experimental EELS L_3 edge and $3s + 3d$ partial DOS of Si crystals.[60] Similarities between black phosphorus and crystalline Si cases are quite remarkable.[60]

Comparison between the EELS L_3 edges collected from four-layer and bulk black phosphorus flakes [Fig. 4(b)] shows relatively small differences. Such small differences can also be seen in the calculated partial DOS as well as the

TABLE I. Black phosphorus lattice parameters determined experimentally and computationally.

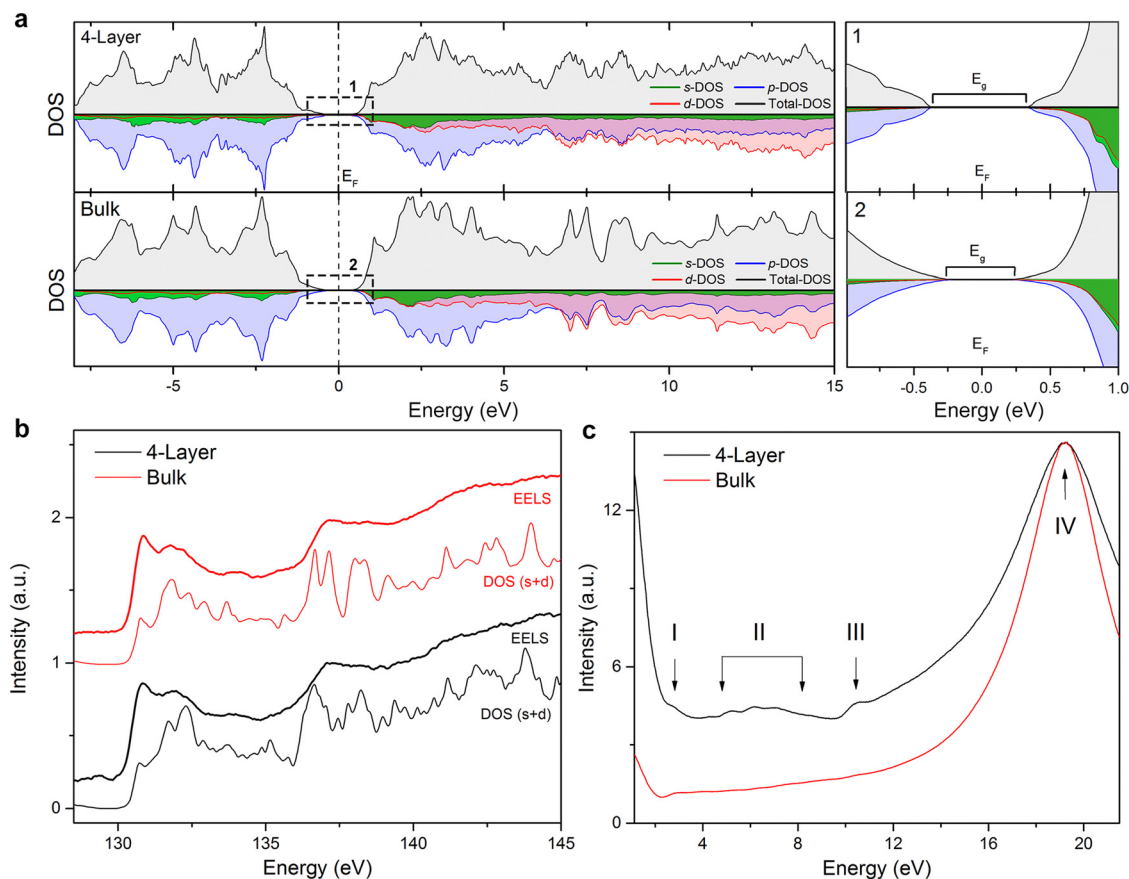|	Lattice parameters (Å)		
Method	a	$b/2$	c
Experiment (ADF-STEM, this work)	3.31(3)	5.4(2)	4.34(5)
Experiment [powder diffraction (Ref. 2)]	3.3136(5)	5.2390(5)	4.3763(5)
Computation (HSE06 + vdW, this work)	3.31	5.39	4.39
Computation (others)	3.34 (Ref. 7)	—	4.47 (Ref. 7)
	3.337 (Ref. 50)	5.367 (Ref. 50)	4.423 (Ref. 50)
	3.3133 (Ref. 43)	5.237 (Ref. 43)	4.374 (Ref. 43)

FIG. 4. (Color online) Electronic structure of black phosphorus. (a) (Left) DOS predicted by *ab initio* calculations for four-layer and bulk black phosphorus. Individual DOS contributions to the valence and conduction bands from $3s$, $3p$, and $3d$ orbitals are shown. Panels on the right show the dotted regions of DOS containing the bandgaps. (b) Monochromated EELS P L_3 edge recorded with 0.25 eV energy resolution with calculated $3s + 3d$ partial DOS, which is broadened with a 0.25 eV FWHM Gaussian function for better comparison. The onset of both experimental EELS P L_3 edge is at 130.3 eV and the calculated partial DOS were aligned accordingly. (c) Low-loss EEL spectra from four-layer and bulk black phosphorus with a strong plasmon peak at 19.3 eV.

band structures from which they are derived (see Fig. S5 in supplementary material). This suggests that the changes in the electronic structure of few-layer black phosphorus over bulk black phosphorus almost saturate at four layers. However, it should be noted that pronounced differences in the band structures of black phosphorus can still be observed between one and three layers (see supplementary material).

Larger changes, as a function of thickness, can be observed in the low-loss EEL spectrum, which predominantly represents the dielectric response of a material to external electromagnetic excitation. As can be seen from Fig. 4(c), whereas bulk plasmon-loss peaks for four-layer and bulk black phosphorus occur at the same energy, $E_{P,max} = 19.3$ eV (feature IV), the peak widths or full width at half-maximums (FWHMs) are significantly different, narrowing from $\Delta E_P = 8.5$ eV for the four-layer sample to 4.9 eV for the bulk. This narrowing corresponds to differences in the plasmon excitation energies, $E_{P,0}^2 = E_{P,max}^2 + [\Delta E_P/2]^2$, and changes in the entire complex dielectric function, $\varepsilon(E) = \varepsilon_1(E) + i\varepsilon_2(E)$, of the material.[42] In addition to the bulk plasmon peak, the low-loss EELS for four-layer black phosphorus also shows distinct features (I, II, and III) in the 1–12 eV energy range that may be characterized by the dominating electronic interband and surface plasmon excitations. Unlike bulk plasmons,

excitations of surface modes in EELS is a more complex function of sample thickness.[42] This behavior is evident in Fig. S7, which contains a low-loss EELS comparison for three-, four-, eight-, 20-layer, and bulk black phosphorus. As the sample becomes thinner, the bulk plasmon peak at 19.3 eV begins to share similar intensities as the features at 5 and 10 eV. To understand the nature of the features in the 1–12 eV energy range, loss functions, Im $\{-1/\varepsilon(E)\}$, originating from interband transitions as well as surface plasmon excitations were calculated for the extreme case of monolayer black phosphorus (see Sec. III for calculation procedure). Figure 5(a) shows the calculated surface plasmon dispersion relation. Due to the highly anisotropic electronic structure of black phosphorus,[8,12] two distinct modes can be observed corresponding to surface plasmon excitations along the *a*- and *c*-directions. Figure 5(b) shows the electron beam scattering cross-section as a function of scattering angle and energy for these surface plasmon modes. Concentrated intensities can be observed near 2 and 10 eV. These modes qualitatively explain features A and F in the measured EEL spectra, as shown in Fig. 5(c). The large peak observed at 10–11 eV in the measured EELS originates from the higher energy surface plasmon mode, whereas feature A is likely the lower energy surface plasmon. Peaks in the DFT-calculated interband
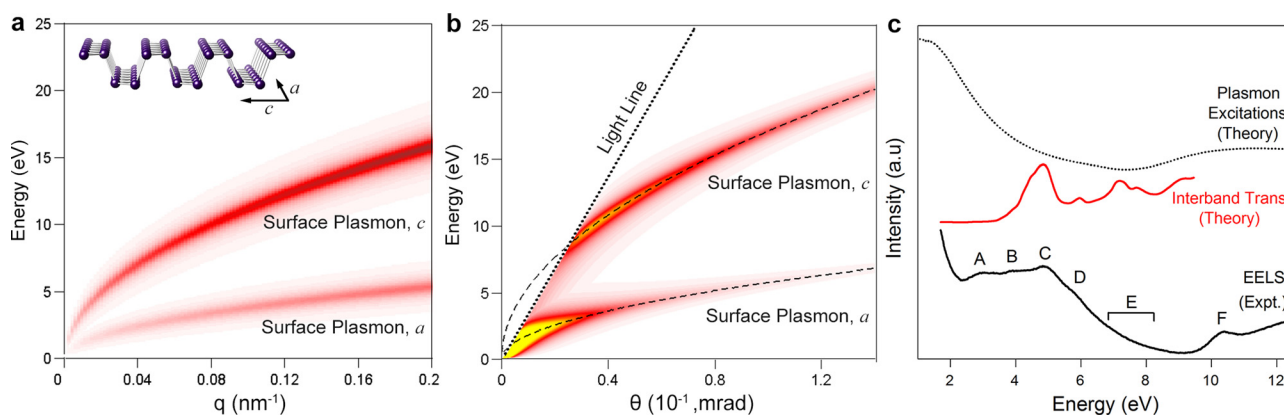
FIG. 5. (Color online) Surface plasmon and interband transitions of black phosphorus. (a) Calculated surface plasmon dispersion relationship for monolayer black phosphorus. The two branches correspond to surface plasmon excitations along the *a*- and *c*-directions. (b) Electron beam scattering cross section, $\frac{\partial^2 \sigma}{\partial E \partial \theta}$, based on the dispersion relationship in (a). (c) Comparison of experimental EELS of three-layer black phosphorus with the calculated loss function, Im $\{-1/\varepsilon(E)\}$, for plasmon excitations and interband transitions.

transitions also match well with peaks B, C, and D in the measured EELS data. Slight quantitative differences between the measured EELS and the calculated loss functions are likely due to a number of reasons: monolayer black phosphorus as opposed to a three-layer black system is used in the experiment (changing the number of layers has been shown to cause slight shifts in surface plasmon energies for other layered materials[61]); higher energy peaks in the interband transitions, such as feature E, are more difficult to resolve due to a lower cross section of scattering;[42] and Cherenkov radiation, which produces a signal in the 1–5 eV region, was not incorporated into the calculations. The complementary results from the measured EELS and calculated loss functions show that both surface plasmon modes as well as interband transitions can indeed be captured here.

D. Effects of oxidation

1. STEM-EDX analysis

A notable limitation of black phosphorus use for the fabrication of FETs and other devices is its susceptibility to oxidation under ambient conditions.[27,28,49] Additional device degradation experiments (see supplementary material) also agreed with the observed oxidation and transport measurements from a previous study by Wood *et al.*[28] In order to understand the nature of the observed oxidation of black phosphorus and its possible influence on device performance, systematic pre- and post-oxidation STEM analyses were performed. Figure 6(a) shows low-magnification ADF-STEM images and associated STEM-EDX maps from a black phosphorus flake before and after 40 h of exposure to ambient conditions. Whereas the preoxidized flake appears pristine in the ADF-STEM images, the postoxidized flake appears to be coated with an additional film with most non-substrate-supported areas etched away. This postoxidation observation bears some resemblance to the BP encapsulated species observed by Wood *et al.* using CTEM.[28] However, the STEM imaging did not show any movement of the surface material, in contrast to observations reported there.

STEM-EDX compositional maps of pre- and postoxidized states of the black phosphorus flake reveals a significant increase in the oxygen content of the flake from 16 to 73 at. %. Because P is threefold coordinated, this initial O atomic percentage suggests that no more than 5%–10% of the pristine black phosphorus flake is oxidized initially. This small amount of oxidation likely occurred during the exfoliation and transfer of the black phosphorus (see Sec. II). It should be noted that another method introduced by Lu *et al.*[62] and later modified by Liu *et al.*[49] may produce specimens with even less oxygen. Quantification of the EDX data (described in detail in supplementary material) shows that the initial and final carbon content remains constant at approximately 3.3 at. %, which indicates that black phosphorus oxidizes by reacting primarily to O_2, and not CO_2, in the presence of water, which was also suggested previously.[21,28] Furthermore, the final atomic percentages of P (24 at. %) and O (73 at. %) were observed to be very close to 1:3, indicating that the final oxidized product is either PO_3 or H_3PO_3, The two compounds cannot be further distinguished using EDX because of the inability to detect hydrogen x-rays. The formation of PO_3 or H_3PO_3 provides experimental clarification about the composition of the P_xO_y compounds proposed to be formed oxidation.[21,27,28] To understand the crystallinity of PO_3 or H_3PO_3, electron beam diffraction experiments were performed. Diffraction patterns from the postoxidized flake shows that the PO_3 or H_3PO_3 is amorphous (see supplementary material for details), which is consistent with the observations by Wood *et al.*[28]

2. STEM-EELS analysis

STEM-EELS measurements performed on pre- and post-oxidized samples provide additional insights for understanding device degradation over time as it is mainly due to changes in the electronic structure of the black phosphorus channel over the oxidation period. Figures 6(b) and 6(c) show the core- and low-loss EEL spectra, respectively, recorded before and after oxidation. The P $L_{2,3}$ core-loss EEL spectrum from $(H_3)PO_3$ shows an onset (feature I) blue
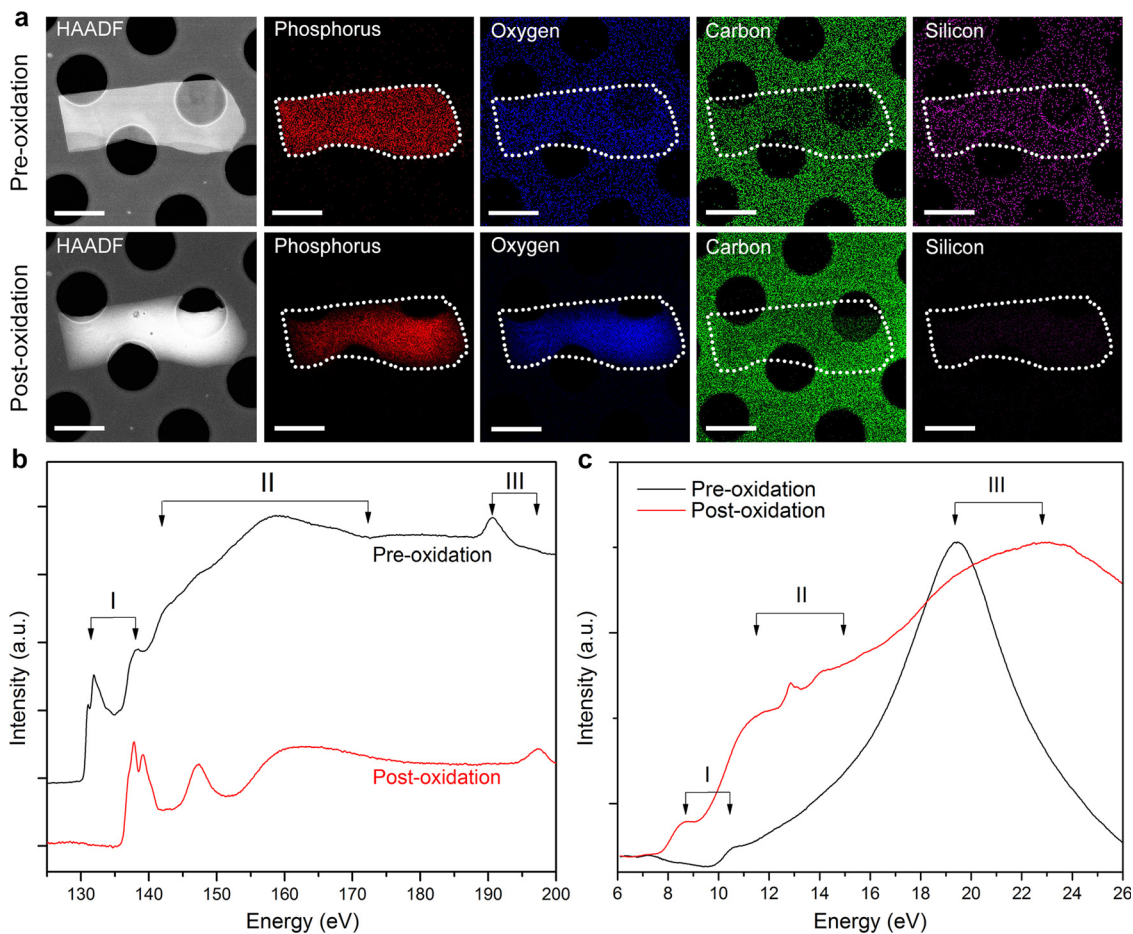
FIG. 6. (Color online) Effects of oxidation of black phosphorus. (a) ADF-STEM images and elemental EDX maps of the same black phosphorus flake before and after oxidation. The ADF-STEM image and composition maps are acquired simultaneously. The white borders in the EDX maps are used to highlight the position of the original flake before oxidation. The scale bars are 1 μm. (b) Core-loss EEL spectra of P $L_{2,3}$ and L_1 edges, and (c) low-loss EEL spectra from a black phosphorus flake before and after oxidation. EDX and EELS data for postoxidation were acquired after 40 h of exposing the preoxidized flake to atmosphere.

shift from 130.3 to 136.1 eV. The EELS fine structure from the oxidized flakes beyond the onset (feature II) shows that the $s + d$ partial DOS of the material has changed significantly. The L_1 edge (feature III) also appears to have blue shifted approximately 6.6 eV as a result of oxidation. The blue shifts of both the $L_{2,3}$ and L_1 edges suggest that oxidation not only alters the details of the band structure of black phosphorus but also results in a bandgap increase of approximately 6 eV, which converts the material from a semiconductor into an insulator. Thus, the degradation of a FET after a period of time likely occurs because the black phosphorus, once fully oxidized, becomes a dielectric $(H_3)PO_3$ that can no longer function as a conductive channel. The core-loss results mainly agree with the STEM-EELS oxidation and thermal stability studies by Liu *et al.*[49] However, the observed shifts and changes in the P $L_{2,3}$ and L_1 edges occurred no less than 24 h after continuous exposure to ambient conditions. Therefore, dramatic changes in the core-loss EEL spectra due to oxidation are unlikely to be observed within 1 h of ambient exposure. Additionally, the measured P $L_{2,3}$ edge of the preoxidized flake in this oxidation study matches the P $L_{2,3}$ edge reported by Liu *et al.*, who used a passivation layer transfer method to minimize oxygen

exposure.[49] This shows that the pristine exfoliated black phosphorus flakes studied in this experiment are largely undamaged and, ultimately, justifies the use of PDMS stamping transfer for this analysis.

The low-loss EEL spectrum from the oxidized black phosphorus shows a significant shift of the bulk plasmon peak (feature III) from 19.3 ± 0.1 eV for the pristine flake to 23.0 ± 0.2 eV for the oxidized flake with peak broadening increasing from 7 ± 1 to 21 ± 1 eV, correspondingly. Other changes also occur in the low-loss EEL spectrum, such as the appearance of features I and II, which can be attributed to changes in the surface plasmon modes and interband electronic excitations. Considering the changes in DOS shown by core-level EELS and the increase in bandgap from semiconducting, crystalline black phosphorus to dielectric, amorphous PO_3 or H_3PO_3, FETs fabricated with black phosphorus would be expected to lose their device capability over time, which is ultimately what is observed in our measurements (see supplementary material) and in previous reports.[21,28]

V. CONCLUSION

In conclusion, this analytical STEM study clarified theoretical predictions on the atomic and electronic structure of

2D black phosphorus and the nature of its oxidation under ambient conditions. For the atomic structure, *ab initio* calculations showed that AB-stacking is the only stable configuration for defect-free black phosphorus, even for the atomically thin exfoliated cases. Experimental ADF-STEM images from three high-symmetry zone axes confirmed the stacking order to be AB and provided the lattice parameters $a = 3.31(3)$ Å, $b/2 = 5.4(2)$ Å, and $c = 4.34(5)$ Å. Furthermore, these experimental ADF-STEM images were consistent with simulated ADF-STEM results. For the electronic structure, the DOS calculated using *ab initio* methods showed excellent agreement with EELS core-loss measurements. EELS core-loss analyses from black phosphorus flakes of various thicknesses showed possible saturation in changes of the electronic properties from thickness as low as 4–5 layers. In addition, calculated loss functions of surface plasmon excitation and interband transitions explained the features observed in low-loss EELS measurements for three-layer black phosphorus. Finally, STEM-EDX and STEM-EELS revealed that amorphous PO_3 or H_3PO_3 forms during the oxidation of black phosphorus. The conduction band DOS, bulk and surface plasmon excitations, and dielectric functions of the PO_3 or H_3PO_3 are all distinctly different from those of pristine black phosphorus. Oxidation appears to be one of the main reasons why devices exposed to atmosphere over time suffer dramatic degradation in their performance.

ACKNOWLEDGMENTS

[1]R. W. Keyes, Phys. Rev. 92, 580 (1953).
[2]A. Brown and R. Stig, Acta Cryst. 19, 684 (1965).
[3]Y. Maruyama, S. Suzuki, K. Kobayashi, and S. Tanuma, Physica B 105, 99 (1981).
[4]A. K. Geim and K. S. Novoselov, Nat. Mater. 6, 183 (2007).
[5]A. K. Geim and I. V. Grigorieva, Nature 499, 419 (2013).
[6]L. Li, Y. Yu, G. J. Ye, Q. Ge, X. Ou, H. Wu, D. Feng, X. H. Chen, and Y. Zhang, Nat. Nanotechnol. 9, 372 (2014).
[7]H. Liu, A. T. Neal, Z. Zhu, Z. Luo, X. Xu, D. Tománek, and P. D. Ye, ACS Nano 8, 4033 (2014).
[8]F. Xia, H. Wang, and Y. Jia, Nat. Commun. 5, 4458 (2014).
[9]M. Buscema, D. J. Groenendijk, G. A. Steele, H. S. J. van der Zant, and A. Castellanos-Gomez, Nat. Commun. 5, 4651 (2014).
[10]S. Das, W. Zhang, M. Demarteau, A. Hoffmann, M. Dubey, and A. Roelofs, Nano Lett. 14, 5733 (2014).
[11]V. Tran, R. Soklaski, Y. Liang, and L. Yang, Phys. Rev. B 89, 235319 (2014).
[12]J. Qiao, X. Kong, Z.-X. Hu, F. Yang, and W. Ji, Nat. Commun. 5, 4475 (2014).
[13]L. Kou, T. Frauenheim, and C. Chen, J. Phys. Chem. Lett. 5, 2675 (2014).
[14]Y. Deng et al., ACS Nano 8, 8292 (2014).
[15]J. Sun, G. Zheng, H.-W. Lee, N. Liu, H. Wang, H. Yao, W. Yang, and Y. Cui, Nano Lett. 14, 4573 (2014).
[16]Y. Du, H. Liu, Y. Deng, and P. D. Ye, ACS Nano 8, 10035 (2014).
[17]R. Hultgren, N. S. Gingrich, and B. E. Warren, J. Chem. Phys. 3, 351 (1935).
[18]T. Takahashi, H. Tokailin, S. Suzuki, T. Sagawa, and I. Shirotani, J. Phys. C 18, 825 (1985).
[19]C. D. Zhang et al., J. Phys. Chem. C 113, 18823 (2009).
[20]S. P. Koenig, R. A. Doganov, H. Schmidt, A. H. Castro Neto, and B. Ozyilmaz, Appl. Phys. Lett. 104, 103106 (2014).
[21]A. Favron et al., "Photooxidation and quantum confinement effects in exfoliated black phosphorus," Nat. Mater. (published online).
[22]A. Castellanos-Gomez et al., 2D Mater. 1, 025001 (2014).
[23]S. Sugai and I. Shirotani, Solid State Commun. 53, 753 (1985).
[24]K. A. Mkhoyan, A. W. Contryman, J. Silcox, D. A. Stewart, G. Eda, C. Mattevi, S. Miller, and M. Chhowalla, Nano Lett. 9, 1058 (2009).
[25]R. J. Nicholls, A. T. Murdock, J. Tsang, J. Britton, T. J. Pennycook, A. Koós, P. D. Nellist, N. Grobert, and J. R. Yates, ACS Nano 7, 7145 (2013).
[26]K. Suenaga, H. Kobayashi, and M. Koshino, Phys. Rev. Lett. 108, 075501 (2012).
[27]A. Ziletti, A. Carvalho, D. K. Campbell, D. F. Coker, and A. H. Castro Neto, Phys. Rev. B 91, 085407 (2014).
[28]J. D. Wood et al., Nano Lett. 14, 6964 (2014).
[29]A. Castellanos-Gomez, M. Buscema, R. Molenaar, V. Singh, L. Janssen, H. S. J. van der Zant, and G. A. Steele, 2D Mater. 1, 011002 (2014).
[30]See supplementary material at http://dx.doi.org/10.1116/1.4926753 for relevant technical procedures on the quantitative treatment of EDX, image processing, and EELS deconvolution; all of which are black phosphorus analytical STEM results presented in the main text. Additionally, device transport measurements and diffraction patterns referenced in the main text is also discussed in detail.
[31]G. Kresse and J. Hafner, Phys. Rev. B 47, 558 (1993).
[32]G. Kresse and J. Hafner, Phys. Rev. B 49, 14251 (1994).
[33]J. Heyd, G. E. Scuseria, and M. Ernzerhof, J. Chem. Phys. 118, 8207 (2003).
[34]J. Perdew, K. Burke, and M. Ernzerhof, Phys. Rev. Lett. 77, 3865 (1996).
[35]J. Paier, M. Marsman, K. Hummer, G. Kresse, I. C. Gerber, and J. G. Ángyán, J. Chem. Phys. 124, 154709 (2006).
[36]K. Hummer, J. Harl, and G. Kresse, Phys. Rev. B 80, 115205 (2009).
[37]A. Tkatchenko and M. Scheffler, Phys. Rev. Lett. 102, 073005 (2009).
[38]G. Kresse and D. Joubert, Phys. Rev. B 59, 1758 (1999).
[39]M. Payne, M. Teter, D. Allan, T. Arias, and J. Joannopoulos, Rev. Mod. Phys. 64, 1045 (1992).
[40]P. Blöchl, O. Jepsen, and O. Andersen, Phys. Rev. B 49, 16223 (1994).
[41]M. Gajdoš, K. Hummer, G. Kresse, J. Furthmüller, and F. Bechstedt, Phys. Rev. B 73, 045112 (2006).
[42]R. F. Egerton, Electron Energy-Loss Spectroscopy in the Electron Microscope, 3rd ed. (Springer, New York, 2011).
[43]T. Low, R. Roldán, H. Wang, F. Xia, P. Avouris, L. M. Moreno, and F. Guinea, Phys. Rev. Lett. 113, 106802 (2014).
[44]A. Morita, Appl. Phys. A 39, 227 (1986).
[45]J. M. Cowley and A. F. Moodie, Acta Crystallogr. 10, 609 (1957).
[46]E. J. Kirkland, Advanced Computing in Electron Microscopy, 2nd ed. (Springer, New York, 2010).
[47]J. Wen et al., Microsc. Microanal. 16, 183 (2010).
[48]A. Mittal, D. B. Zhang, C. Teresi, T. Dumitrica, and K. A. Mkhoyan, Phys. Rev. B 84, 153401 (2011).
[49]X. Liu, J. D. Wood, K.-S. Chen, E. Cho, and M. C. Hersam, J. Phys. Chem. Lett. 6, 773 (2015).
[50]S. Hillyard, R. F. Loane, and J. Silcox, Ultramicroscopy 49, 14 (1993).
[51]J. Dai and X. C. Zeng, J. Phys. Chem. Lett. 5, 1289 (2014).
[52]C. H. Lui, Z. Li, Z. Chen, P. V. Klimov, L. E. Brus, and T. F. Heinz, Nano Lett. 11, 164 (2011).
[53]J. Lin, W. Fang, W. Zhou, A. R. Lupini, J. C. Idrobo, J. Kong, S. J. Pennycook, and S. T. Pantelides, Nano Lett. 13, 3262 (2013).
[54]S. J. Pennycook and L. A. Boatner, Nature 336, 565 (1988).
[55]Y. Li, S. Yang, and J. Li, J. Phys. Chem. C 118, 23970 (2014).

[56]V. V. Ivanovskaya, P. Wagner, A. Zobelli, I. Suarez-Martinez, A. Yaya, and C. P. Ewels, *GraphITA 2011* (Springer, Berlin, Heidelberg, 2012), pp. 75–85.

[57]D. Liu, W. Lei, S. Qin, and Y. Chen, Sci. Rep. **4**, 4453 (2014).

[58]D. A. Muller, D. J. Singh, and J. Silcox, Phys. Rev. B **57**, 8181 (1998).

[59]X. Ling, H. Wang, S. Huang, F. Xia, and M. S. Dresselhaus, Proc. Natl. Acad. Sci. U.S.A. **112**, 4523 (2015).

[60]P. E. Batson, J. Electron Microsc. **45**, 51 (1996).

[61]P. Johari and V. B. Shenoy, ACS Nano **5**, 5903 (2011).

[62]W. Lu *et al.*, Nano Res. **7**, 853 (2014).